Geophys. J. Int. (1996) **125**, 545–558

Wave diffraction in multilayered media with the Indirect Boundary Element Method: application to 3-D diffraction of long-period surface waves by 2-D lithospheric structures

H. A. Pedersen,[1] V. Maupin,[2] and M. Campillo[1,3]

[1] *Laboratoire de Géophysique Interne et Tectonophysique de Grenoble, University of Grenoble, BP* 53x, 38041 *Grenoble Cedex, France*
[2] *Institutt for Geofysikk, University of Oslo,* PO Box 1022, *Blindern,* 0315 *Oslo, Norway*
[3] *Institut Universitaire de France*

Accepted 1995 December 21. Received 1995 November 14; in original form 1995 August 3

SUMMARY

An indirect boundary-element method is presented for simulating seismic wave diffraction in layered media with irregular interfaces. Recursive formulae are developed to take into account an arbitrary number of layers without increasing the size of the problem in terms of computer memory. The interfaces between layers are of variable geometry, and interfaces can be superposed to introduce horizontally finite structures, such as lenses or sedimentary basins. In the present implementation, we study three-dimensional (3-D) diffraction of plane waves by two-dimensional (2-D) structures. The formulation is nevertheless sufficiently general to include the complete 3-D case. Even though the method can be used at all scales, the main purpose of the theoretical development is to simulate diffraction of long-period surface waves by heterogeneous lithospheric structures. A new approach to treat incident surface waves in multilayered media is therefore developed, but other wave types, such as body-waves and internal seismic sources, can easily be introduced. The method is verified by transparency tests and comparison with other simulation methods. The application on the 3-D diffraction of plane Rayleigh waves by a major lithospheric boundary shows that significant conversions between wave types are present, and that the diffracted waves influence the apparent phase velocities measured at the surface above the heterogeneity and several wavelengths behind it.

Key words: Boundary Element Method, layered media, lithosphere, surface waves.

INTRODUCTION

Recent developments of regional seismic arrays have provided increasing evidence of strong heterogeneities in the upper mantle (for a review, see Nolet, Grand & Kennett 1994). Analysis of data from these arrays is still limited because of our present lack of knowledge on wave diffraction by such heterogeneities. Surface waves are especially difficult to interpret when strong heterogeneities are present. These waves nevertheless have a great potential in regional lithospheric studies because they are very sensitive to the rock rigidity, and therefore to thermal anomalies and partial melting.

Several methods are used to study surface-wave diffraction by lithospheric structures, and they have all contributed to a better understanding of surface-wave diffraction. *Perturbation methods* have the advantage of taking into account smooth velocity changes and have been used for both forward and inverse modelling (e.g. Kennett 1984; Woodhouse & Dziewonski 1984; Snieder 1986). On the other hand, their use is restricted to rather small variations in the elastic parameters relative to plane-layered or radially layered reference models. *Local mode-coupling methods* (e.g. McGarr & Alsop 1967; Gregersen 1978; Maupin 1988) have also been used. They are based on the local representation of the seismic waves by a superposition of 'local modes', i.e. the normal modes which would be present in a plane-layered structure with the local elastic parameters as a function of depth. The problem of these methods is primarily that the body waves cannot easily be taken into account in the wavefield representation. Stange & Friederich (1992a,b) propose, in the case of a waveguide, to complement the normal modal set by modes with complex wavenumbers, thus obtaining a complete representation of the wavefield in terms of modes. This *exact solution* can be very useful in simple models, but it is still of limited use for practical purposes. *Finite-difference* and *finite-element methods* (e.g. Lysmer & Drake 1972; Drake & Bolt 1989; Fitas & Mendes-Victor 1992; Cao & Muirhead 1993) present other possibilities for the study of diffraction of surface waves. These methods

are best adapted to smoothly varying media, but they can incorporate geometrically complex models with rather high velocity anomalies. With the finite-difference method, a significant numerical dispersion may occur that is very difficult to separate from the natural dispersion of surface waves.

We present here the extension of another method, the Indirect Boundary Element Method (IBEM), to study surface-wave diffraction by heterogeneities in the lithosphere. We describe the characteristics of IBEM that are necessary to understand the main advantages of the method. For a detailed discussion of IBEM, we refer to Sánchez-Sesma & Luzón (1995).

IBEM is a convenient method to simulate wave diffraction in strongly heterogeneous media. In IBEM, the seismic waves are represented as the radiation from a continuous source distribution on the interfaces of the irregular model. The wavefield representation is complete, i.e. both surface-wave and body-wave parts of the diffracted wavefield are taken into account. No approximations are made in IBEM, except for the discretization of the model interfaces. This discretization replaces the continuous source distribution with elements, each of which has a constant source amplitude.

IBEM is usually used to study site effects across simple superficial structures such as sedimentary basins and surface topography (e.g. Pei & Papageorgiou 1993; Sánchez-Sesma, Ramos-Martinez & Campillo 1993; Pedersen, Sánchez-Sesma & Campillo 1994; Pedersen, Campillo & Sánchez-Sesma 1995). The use of IBEM to interpret seismic data makes it necessary to generalize it, so more realistic earth structures can be considered. We present a generalization of IBEM that is able to simulate surface-wave diffraction by strong heterogeneities in the lithosphere. The development includes two elements. First, we introduce a propagator matrix, which makes it possible to treat models with a large number of irregular layers without increasing the sizes of the matrices to be inverted during the calculation. Second, we develop a formulation to introduce surface waves in such multilayered models.

The development of propagator matrices is a generalization of the propagator matrices proposed by Bouchon, Campillo & Gaffet (1989). It is nevertheless important at this point to note the main differences between their and our approach. First, we use a general formulation that makes it possible to introduce displacements and tractions due to the incident waves in all layers of the model, which is necessary to introduce surface waves. Second, the formulation can be used for 2-D or 3-D simulation problems, while Bouchon *et al.* (1989) treat the 2-D *SH* case. Finally, we use analytical full-space Green's functions in the implementation of the method, while Bouchon *et al.* (1989) calculate Green's functions by the discrete wavenumber approach. In practice, the use of analytical Green's functions makes it possible to integrate analytically the near field on or close to each interface segment.

Very different applications of the method presented can be considered because the determining parameter in the calculation, along with the elastic parameters of the model, is the ratio between the wavelength and the heterogeneity. There is a large choice of type of incident waves: body-waves, single-mode surface waves, superposition of surface-wave modes, and internal sources. There are very few restrictions on the model geometry as a model can contain an arbitrary number of layers. Each layer is homogeneous, so the lateral variation resides in the shape of the interface between layers. There are no restrictions of the variations of elastic parameters across interfaces, and two interfaces can be merged in places to create, for example, lens structures. The formulation is kept general, but the application that we present uses 2-D models, with the possibility of considering obliquely incident plane waves.

This paper is organized as follows. In the first part of the paper we present the method of calculation. In the second part of the paper we present different verifications of the method. Finally, in the third part, we present an example of calculations of 3-D diffraction of plane surface waves incident on a sharp transition zone in the upper mantle.

METHOD

In this section, we present all the necessary elements for the development of the simulation method. In the first subsection, we present the basic integral equations that are used in IBEM and the principles behind the method. The generalization of IBEM to multilayered media is presented in the following subsection by introducing the notations that we use to treat the problem of multilayered media, stating the boundary conditions applied to the problem, and deriving the propagation matrices that are used. Finally, we discuss how to introduce the incoming wavefield, with special emphasis on surface waves.

Basic principles of the Indirect Boundary Element Method (IBEM)

We present here only the very basic theory behind IBEM and we refer the reader to e.g. Sánchez-Sesma & Campillo (1993) or Sánchez-Sesma & Luzón (1995) for further details on the method.

IBEM is based on the Somigliana representation theorem for elastic media (e.g. Aki & Richards 1980). We use a derivation of this theorem (e.g. Sánchez-Sesma & Campillo 1991), which states that in the absence of volume forces, the displacement at any point in a volume V surrounded by the surface S can be expressed as an integral over S:

$$u_i(\mathbf{x}) = \int_S \psi_j(\zeta)\, G_{ij}(\mathbf{x}, \zeta)\, dS_\zeta, \tag{1}$$

where $u_i(\mathbf{x})$ is the displacement in direction i at point $\mathbf{x}$, and $G_{ij}(\mathbf{x}, \zeta)$ is the displacement Green's function, i.e. the displacement in direction i at point $\mathbf{x}$ due to a point source in direction j applied at point ζ. $\psi_j(\zeta)$ is the force density in direction j at ζ. $\psi_j(\zeta)\, dS_\zeta$ is therefore a force distribution on S. Eq. (1) shows that if the Green's functions are known, one simply needs to find the force density ψ_j on the surface S to calculate the displacement at any point in V. Furthermore, the displacement field is continuous across S if ψ_j is continuous on S (Kupradze 1963). When displacements u_i are known, it is possible to calculate stresses and tractions by applying Hooke's law.

Special care must be taken at the singularity $\mathbf{x} = \zeta$, i.e. at the point of application of the force. Kupradze (1963) shows that the contribution to the traction of the singularity of the Green's function equals half the applied force (assuming a smooth boundary). This leads to the following integral equation for tractions:

$$t_i(\mathbf{x}) = c\psi_i(\mathbf{x}) + \int_S \psi_j(\zeta)\, T_{ij}(\mathbf{x}, \zeta)\, dS_\zeta, \tag{2}$$

where c equals 0 if $\mathbf{x}$ is outside S, c equals 1/2 if $\mathbf{x}$ tends to S from the inside of V, and c equals $-1/2$ if $\mathbf{x}$ tends to S from the outside of V. $t_i(\mathbf{x})$ is the traction (on the surface S) in direction i at point $\mathbf{x}$; $T_{ij}(\mathbf{x},\boldsymbol{\zeta})$ is the traction Green's function, i.e. the traction in direction i at point $\mathbf{x}$ on interface S due to a point source in direction j applied at point $\boldsymbol{\zeta}$.

It is usual to consider the total wavefield as the superposition of the so-called *free field* (due to the incident waves) and the so-called *diffracted waves*,

$$u_i^{\mathrm{E}} = u_i^{\mathrm{o}} + u_i^{\mathrm{d}}, \tag{3}$$

where u_i^{E} is the total displacement, u_i^{o} the free-field displacement, and u_i^{d} is the displacement of the diffracted waves. The definition of the free field can vary, but it is often defined as the wavefield in the absence of any heterogeneity. The scattered wavefield is therefore defined as the one which satisfies all boundary conditions for the total wavefield. For a more complete discussion, we refer to Sánchez-Sesma & Luzón (1995). In this subsection we do not yet precisely define the free field to keep the theoretical developments as general as possible.

To solve the problem numerically, the surface S is discretized into K elements, with a constant surface force density on each element. The discrete version of eq. (1), including the free-field term, is

$$u_i(\mathbf{x}) = u_i^{\mathrm{o}}(\mathbf{x}) + \sum_{k=1}^{K} \psi_j(\zeta_k) g_{ij}(\mathbf{x}, \zeta_k) \qquad k=1, \mathrm{K}, \tag{4a}$$

with

$$g_{ij}(\mathbf{x}, \zeta_k) = \int_{\zeta_k - \Delta s_k/2}^{\zeta_k + \Delta s_k/2} G_{ij}(\mathbf{x}, \zeta_k)\, dS_\zeta, \tag{4b}$$

and the discrete version of eq. (2) is

$$t_i(\mathbf{x}_n) = t_i^{\mathrm{o}}(\mathbf{x}_n) + \sum_{k=1}^{K} \psi_j(\zeta_k) t_{ij}(\mathbf{x}_n, \zeta_k) \qquad k=1, \mathrm{K}, \tag{5a}$$

with

$$t_{ij}(\mathbf{x}_n, \zeta_k) = \frac{1}{2}\delta_{ij}\delta_{nk} + \int_{\zeta_k - \Delta s_k/2}^{\zeta_k + \Delta s_k/2} T_{ij}(\mathbf{x}_n, \zeta_k)\, dS_\zeta, \tag{5b}$$

where u^0 and t^0 are the displacements and tractions of the free field, Δs_k is the length of the kth surface element and δ is the Kronecker symbol. These discrete sums are good approximations to the continuous integrals if the segments are small compared to the wavelength and sufficiently small to represent the geometry of S well. In the applications presented in this paper, we use five segments per wavelength. It is possible to reduce the discretization to three to four segments per wavelength without significant loss of precision.

Generalization to multilayered media

Notations

We use here basically the same notations as Bouchon *et al.* (1989), with some modifications to increase the clarity of the development, and with some new elements. Fig. 1 shows the geometry of the problem: $N+1$ layers (including the half-space) are separated by N irregular interfaces. The upper layer is delimited by the free surface. The layers are numbered from 1 (uppermost layer) to $N+1$ (half-space) and the interfaces are numbered from 1 (uppermost interface) to N (deepest interface). The free surface carries interface number 0.

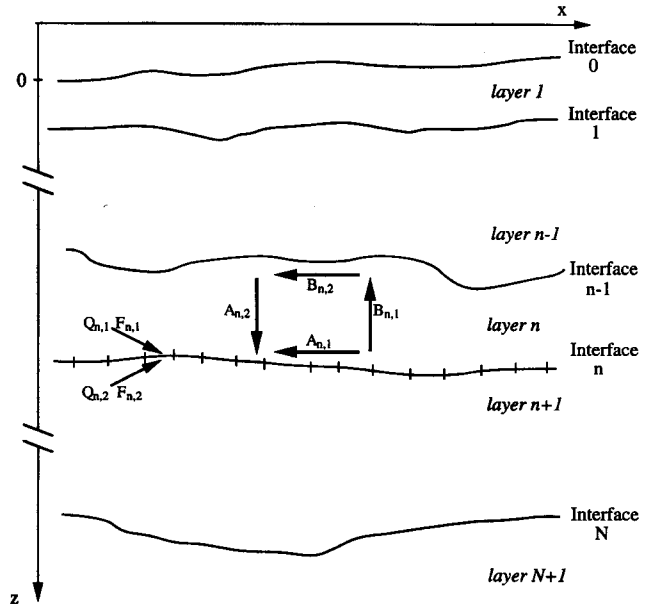

Figure 1. Model configuration. $N+1$ layers are separated by N interfaces, of which each is discretized into K_n segments. The bold arrows indicate displacement–traction matrices and the thin arrows indicate sources and free-field vectors.

K_n surface forces $\mathbf{Q}$ are distributed on each interface n. In fact, there are two such sets of surface forces on each interface: one with forces radiating energy into the layer above the interface and another with forces radiating energy into the layer below. We write the sources on one side, j, of the interface, n, in a vector, $\mathbf{Q}_{n,j}$ (of length $3K_n$),

$$\mathbf{Q}_{n,j} = [Q_{i=1}^{n,j}(\mathbf{x}_1), \ldots, Q_{i=1}^{n,j}(\mathbf{x}_{K_n}), Q_{i=2}^{n,j}(\mathbf{x}_1), \ldots, \ldots, Q_{i=3}^{n,j}(\mathbf{x}_{K_n})], \tag{6a}$$

where n ($n=0,N$) is the interface number, $\mathbf{x}_k$ ($k=1,K_n$) is the source position on the interface, and i ($i=1,2,3$) is the component of the point source. j is used to distinguish whether the source radiates energy into the layer above ($j=1$) or into the layer below ($j=2$).

In the following calculations we also use a vector, $\mathbf{Q}_n$ (of length $6K_n$), containing all the sources on the interface n:

$$\mathbf{Q}_n = [\mathbf{Q}_{n,1}; \mathbf{Q}_{n,2}]. \tag{6b}$$

Here, and in the following equations, the semicolon indicates horizontal attachment of vectors.

At all interfaces we express the displacement and traction at point $\mathbf{x}_k$ by eqs (4) and (5), and we use displacement–traction vectors and matrices. The displacement–traction vector $\mathbf{S}$ (of length $6K_n$) at an interface n is

$$\boldsymbol{S} = [\boldsymbol{u}; \boldsymbol{t}], \tag{7a}$$

with

$$\boldsymbol{u} = [u_1(\mathbf{x}_1), \ldots, u_1(\mathbf{x}_{K_n}), u_2(\mathbf{x}_1), \ldots, u_2(\mathbf{x}_{K_n}), u_3(\mathbf{x}_1), \ldots, u_3(\mathbf{x}_{K_n})], \tag{7b}$$

$$\boldsymbol{t} = [t_1(\mathbf{x}_1), \ldots, t_1(\mathbf{x}_{K_n}), t_2(\mathbf{x}_1), \ldots, t_2(\mathbf{x}_{K_n}), t_3(\mathbf{x}_1), \ldots, t_3(\mathbf{x}_{K_n})]. \tag{7c}$$

In each layer n, the Green's functions can be used to define

four displacement–traction matrices, $\mathbf{A}_{n,1}$, $\mathbf{A}_{n,2}$, $\mathbf{B}_{n,1}$ and $\mathbf{B}_{n,2}$, of the form

$$\begin{bmatrix} \mathcal{G} \\ \mathcal{T} \end{bmatrix}, \tag{8a}$$

with

$$\mathcal{G} = \begin{bmatrix} \mathcal{G}11 & \mathcal{G}12 & \mathcal{G}13 \\ \mathcal{G}21 & \mathcal{G}22 & \mathcal{G}23 \\ \mathcal{G}31 & \mathcal{G}32 & \mathcal{G}33 \end{bmatrix}, \tag{8b}$$

$$\mathcal{T} = \begin{bmatrix} \mathcal{T}11 & \mathcal{T}12 & \mathcal{T}13 \\ \mathcal{T}21 & \mathcal{T}22 & \mathcal{T}23 \\ \mathcal{T}31 & \mathcal{T}32 & \mathcal{T}33 \end{bmatrix}, \tag{8c}$$

where $\mathcal{G}ij$ and $\mathcal{T}ij$ are $K \times K$ matrices, for which each element is:

$$(\mathcal{G}ij)_{rc} = g_{ij}(\mathbf{x}_r, \zeta_c), \tag{8d}$$

$$(\mathcal{T}ij)_{rc} = t_{ij}(\mathbf{x}_r, \zeta_c). \tag{8e}$$

As sketched in Fig. 1, each element of the matrices **A** and **B** expresses the displacement–traction on an interface due to a force on the same or the other interface of the layer. More precisely:

$\mathbf{A}_{n,1}$ (of dimension $6K_n \times 3K_n$) contains the displacements and tractions at interface n due to the sources $\mathbf{Q}_{n,1}$ on interface n;

$\mathbf{A}_{n,2}$ (of dimension $6K_n \times 3K_{n-1}$) contains the displacements and tractions at interface n due to the sources $\mathbf{Q}_{n-1,2}$ on interface $n-1$;

$\mathbf{B}_{n,1}$ (of dimension $6K_{n-1} \times 3K_n$) contains the displacements and tractions at interface $n-1$ due to the sources $\mathbf{Q}_{n,1}$ on interface n;

$\mathbf{B}_{n,2}$ (of dimension $6K_{n-1} \times 3K_{n-1}$) contains the displacements and tractions at interface $n-1$ due to the sources $\mathbf{Q}_{n-1,2}$ on interface $n-1$.

On the nth interface we define the displacement–traction vector $\mathbf{F}$ of the free field by:

$\mathbf{F}_{n,1}$: displacement–traction vector (of dimension $6K_n$) of the free field on the upper side of the interface (in layer n);

$\mathbf{F}_{n,2}$: displacement−traction vector (of dimension $6K_n$) of the free field on the lower side of the interface (in layer $n+1$).

Boundary conditions

Continuity of displacements and tractions at the nth interface can be expressed by

$$\mathbf{A}_{n,2}\mathbf{Q}^{\mathrm{T}}_{n-1,2} + \mathbf{A}_{n,1}\mathbf{Q}^{\mathrm{T}}_{n,1} + \mathbf{F}^{\mathrm{T}}_{n,1} = \mathbf{B}_{n+1,2}\mathbf{Q}^{\mathrm{T}}_{n,2} + \mathbf{B}_{n+1,1}\mathbf{Q}^{\mathrm{T}}_{n+1,1} + \mathbf{F}^{\mathrm{T}}_{n,2}, \tag{9}$$

where superscript T indicates the transposed matrix or vector.

At the deepest interface (N), these conditions become

$$\mathbf{A}_{N,2}\mathbf{Q}^{\mathrm{T}}_{N-1,2} + \mathbf{A}_{N,1}\mathbf{Q}^{\mathrm{T}}_{N,1} + \mathbf{F}^{\mathrm{T}}_{N,1} = \mathbf{B}_{N+1,2}\mathbf{Q}^{\mathrm{T}}_{N,2} + \mathbf{F}^{\mathrm{T}}_{N,2}, \tag{10}$$

and at the free surface, tractions are zero,

$$\mathbf{B}^{\mathrm{inf}}_{1,2}\mathbf{Q}^{\mathrm{T}}_{0,2} + \mathbf{B}^{\mathrm{inf}}_{1,1}\mathbf{Q}^{\mathrm{T}}_{1,1} + \mathbf{F}^{\mathrm{inf}\,\mathrm{T}}_{0,2} = 0, \tag{11a}$$

and displacements are given by

$$\mathbf{u} = \mathbf{B}^{\mathrm{sup}}_{1,2}\mathbf{Q}^{\mathrm{T}}_{0,2} + \mathbf{B}^{\mathrm{sup}}_{1,1}\mathbf{Q}^{\mathrm{T}}_{1,1} + \mathbf{F}^{\mathrm{supT}}_{0,2}. \tag{11b}$$

The superscripts 'inf' and 'sup' indicate that the lower or upper half of the matrices are used. For the displacement–traction matrices, 'inf' corresponds to the traction part and 'sup' to the displacement part.

Note that it is only necessary to know the amplitude of the surface forces at the free surface ($\mathbf{Q}_{0,2}$) and on the top side of the first interface ($\mathbf{Q}_{1,1}$) to calculate displacements at the free surface. We propagate boundary conditions from the deepest interface up to the shallowest one to find these two surface-force distributions. The boundary conditions can, in fact, be propagated upwards by recursive formulae.

Propagation of boundary conditions

Rearrangement of eq. (9) yields

$$\mathbf{A}_{n,2}\mathbf{Q}^{\mathrm{T}}_{n-1,2} = [-\mathbf{A}_{n,1}\mathbf{B}_{n+1,2}]\mathbf{Q}^{T}_{n} + \mathbf{B}_{n+1,1}\mathbf{Q}^{T}_{n+1,1} + \Delta\mathbf{F}^{\mathrm{T}}_{n}, \tag{12a}$$

where

$$\Delta\mathbf{F}_n = \mathbf{F}_{n,2} - \mathbf{F}_{n,1}. \tag{12b}$$

This equation is a recursive formula for the force on the lower side of interface $n-1$ as a function of the forces on interfaces n and $n+1$, and the free field on interface n. We will now show that we can reorganize this recursive formula to one acting on indirect quantities. Let us suppose that we can write eq. (12a) in the form

$$\mathbf{A}_{n,2}\mathbf{Q}^{\mathrm{T}}_{n-1,2} = \mathbf{D}_n\mathbf{Q}^{\mathrm{T}}_{n} + \mathbf{E}^{\mathrm{T}}_{n}, \tag{13}$$

where $\mathbf{D}_n$ and $\mathbf{E}_n$ are some propagator matrices. Eq. (13) applied on layer $n+1$ yields

$$\mathbf{Q}^{T}_{n+1} = \mathbf{D}^{-1}_{n+1}(\mathbf{A}_{n+1,2}\mathbf{Q}^{\mathrm{T}}_{n,2} - \mathbf{E}^{\mathrm{T}}_{n+1}). \tag{14}$$

Insertion of eq. (14) in eq. (12) yields

$$\mathbf{A}_{n,2}\mathbf{Q}^{\mathrm{T}}_{n-1,2} = [-\mathbf{A}_{n,1};\ \mathbf{B}_{n+1,2} + \mathbf{B}_{n+1,1}\,(\mathbf{D}^{-1}_{n+1})^{\mathrm{sup}}\mathbf{A}_{n+1,2}]\,\mathbf{Q}^{\mathrm{T}}_{n} - \mathbf{B}_{n+1,1}(\mathbf{D}^{-1}_{n+1})^{\mathrm{sup}}\mathbf{E}^{\mathrm{T}}_{n+1} + \Delta\mathbf{F}^{\mathrm{T}}_{n}. \tag{15}$$

By simple identification of terms, we find that eq. (13) is equivalent to eq. (12a) if we use

$$\mathbf{D}_n = [-\mathbf{A}_{n,1};\ \mathbf{B}_{n+1,2} + \mathbf{B}_{n+1,1}\,(\mathbf{D}^{-1}_{n+1})^{\mathrm{sup}}\mathbf{A}_{n+1,2}], \tag{16}$$

$$\mathbf{E}^{T}_{n} = -\mathbf{B}_{n+1,1}(\mathbf{D}^{-1}_{n+1})^{\mathrm{sup}}\mathbf{E}^{\mathrm{T}}_{n+1} + \Delta\mathbf{F}^{\mathrm{T}}_{n}. \tag{17}$$

At the deepest interface, eq. (10) can be written as

$$\mathbf{A}_{N,2}\mathbf{Q}^{\mathrm{T}}_{N-1,2} = [-\mathbf{A}_{N,1};\ \mathbf{B}_{N+1,2}]\mathbf{Q}^{\mathrm{T}}_{N} + \Delta\mathbf{F}^{\mathrm{T}}_{N}, \tag{18}$$

which provides the initial conditions

$$\mathbf{D}_N = [-\mathbf{A}_{N,1};\ \mathbf{B}_{N+1,2}], \tag{19}$$

$$\mathbf{E}_N = \Delta\mathbf{F}_N, \tag{20}$$

for the recursive formulae (16) and (17). Note that we have obtained recursive relations for $\mathbf{D}_n$ and $\mathbf{E}_n$ that do not involve directly the forces $\mathbf{Q}_n$. Starting from the initial values $\mathbf{D}_N$ and $\mathbf{E}_N$, we use eqs (16) and (17) to propagate the matrices $\mathbf{D}_n$ and $\mathbf{E}_n$ upwards. As long as we are not directly interested in the wavefield at depth, we do not need to calculate the forces before we have come to the last step of the recursive relation in the top layer of the model. There, application of boundary conditions at the first interface [eq. (13) with $n=1$] and at the free surface (eq. 11a) makes it possible to construct a system of linear equations,

$$\mathbf{C}\mathbf{x}^{\mathrm{T}} = \mathbf{y}^{\mathrm{T}}, \tag{21}$$

with

$$\mathbf{C}=\begin{bmatrix} -\mathbf{D}_1^{\text{left}} & -\mathbf{D}_1^{\text{right}} & \mathbf{A}_{1,2} \\ \mathbf{B}_{1,1}^{\text{inf}} & 0 & \mathbf{B}_{1,2}^{\text{inf}} \end{bmatrix} \tag{21a}$$

$$\mathbf{x}=[\mathbf{Q}_{1,1};\ \mathbf{Q}_{1,2};\ \mathbf{Q}_{0,2}], \tag{21b}$$

$$\mathbf{y}=[\mathbf{E}_1;\ -\mathbf{F}_{0,2}^{\text{inf}}]. \tag{21c}$$

C is a square invertible matrix and **y** is completely known. Solving eq. (21) yields the force distributions $\mathbf{Q}_{0,2}$ and $\mathbf{Q}_{1,1}$. At any point in the first layer or at the surface, the displacement can then be found by eq. (11b).

The recursive formulae offer an alternative to a global inversion aimed at finding all surface forces simultaneously. The size of the matrix in the global approach is, for realistic models, too big to be inverted on most present-day computers. The biggest matrix, **C**, is square with $(6\times K_1+3\times K_0)$ lines, i.e. no more than if a global approach is applied to a model with one irregular layer over a half-space. The number of operations of the simulation, and therefore the computation time, increases approximately linearly with the number of layers in the model.

Implementation and introduction of the free field

The equations developed above are generic, in that we have put no limitations on the Green's functions, so it is possible to use them to treat 2-D or 3-D problems and to use Green's functions, for example, for anisotropic media, and also in that there are no restrictions on the nature of the incident waves. We present here the implementation of the method for certain classes of models and certain types of incoming waves.

First, we use full-space Green's functions for isotropic and homogeneous media. This implies that each layer is homogeneous and isotropic. Use of full-space Green's functions will introduce model truncation effects because the model in practice is of limited horizontal extent so spurious waves will be reflected back into the model. It is therefore necessary to extend the model to a sufficient distance for these artificial waves to arrive later in the seismograms than the 'real' waves in the model. We introduce absorbing boundaries (by using very low Q values in the calculation of the Green's functions for sources in a boundary zone next to the edge of the model) to minimize model truncation effects. When the wavelengths considered are smaller than the absorbing zones, this technique is very efficient at eliminating the emission of reflected waves at the model limits.

Second, we study the 3-D scattering by 2-D structures, i.e. plane waves incident on a 2-D structure with arbitrary azimuth and incidence angle. The precise geometry is shown in Fig. 2, where azimuth and incidence are defined. We use Green's functions in the frequency domain for this geometry (Pedersen *et al.* 1994), and the diffraction is 3-D with coupling of all wave types. The formulation of the problem in the frequency domain implies that synthetic seismograms are obtained by a Fourier transform after multiplication with a source function.

Finally, the waves incident on the structure are either body waves, incident from below, or surface waves. Incident body waves are used here only to verify the simulation method (see next section). The free field for body waves may be introduced in a very simple way, by calculating the displacements and tractions produced by the wave when it hits the structure at the deepest interface ($\Delta\mathbf{F}_n=0$ for $n\neq N$). The field higher up in the structure is then calculated by propagating the free field upwards with the recursive formulae.

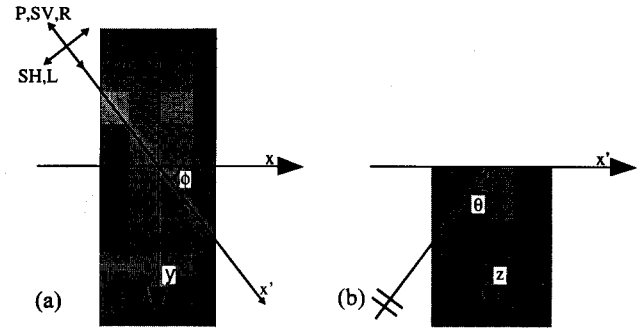

Figure 2. Definition of azimuth and incidence angles of the incident plane waves. The shaded area delimits the laterally heterogeneous zone. (a) The azimuth ϕ is defined in the horizontal plane as the angle between the propagation direction of the incoming waves and the x axis. (b) The incidence angle θ is defined in the vertical plane as the angle between the propagation direction of the incoming waves and the z axis.

Surface waves, the diffraction of which is the main scope of this work, are incident upon the model from the side. The free field must therefore be distributed at all depths, and we need to define the free field more precisely. Since the method involves surface forces but no internal body forces in the layers, the free field must be a solution to the wave equation inside each layer. On the other hand, it may be discontinuous on the interfaces. The analytical continuation of the field in a well-chosen, laterally homogeneous reference model has these two properties. We therefore use it as the free field for surface waves. We discuss here how the reference model must be chosen, and recall what the analytical continuation of a field is.

In order to be used in connection with the analytical continuation, the reference model must be composed of all the layers of the laterally varying model, with the same elastic parameters, but possibly other thicknesses. Here we use flat layers for the reference model. We can choose layer thicknesses that are the most convenient for the computation of the diffracted field. Some layers may have null thickness, such as those that become lenses in the laterally varying model. In practice, we use the thicknesses of the layers on the side of the laterally varying model on which the surface waves are incident, so their propagation is described in terms of normal modes. If necessary, null-thickness layers are inserted for lenses or for layers existing only on the other side of the heterogeneous model. The flat-layered part of the model located behind the laterally heterogeneous part of the model can be different from the reference structure.

In the flat reference model, a surface-wave mode can be described in each homogeneous layer either by a displacement–tension vector function of depth, or by the amplitudes of up- and downgoing or inhomogeneous body waves (e.g. Ben Menahem & Singh 1981). In each homogeneous layer, the displacement–traction of Love waves can be described by only two amplitudes: one for the upgoing *SH* wave and one for the downgoing *SH* wave. For Rayleigh waves, there are four amplitudes in each layer: two for *P* waves and two for *SV* waves. The displacement–traction needs to be known only at one depth in the layer to calculate the amplitudes. On the other hand, the displacement–traction at any depth in the

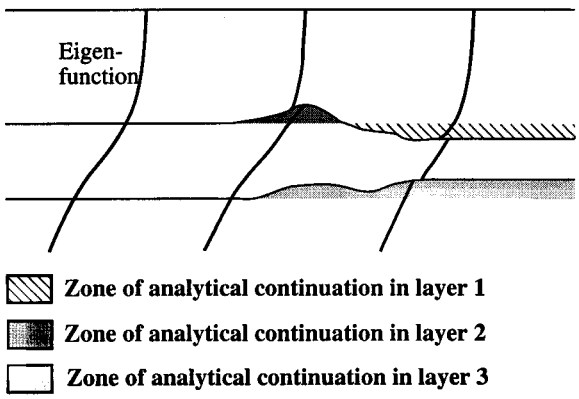

Figure 3. Introduction of surface waves in a laterally heterogeneous model. The surface waves are incident from the left, where their eigenfunctions (represented by bold lines) are continuous and fulfil all boundary conditions. In the laterally heterogeneous part of the model, the expressions for upgoing and downgoing body waves are extended analytically, inducing discontinuities across the interfaces. Three zones of analytical continuation exist in this model. These zones are shown by different grey scales.

layer can be readily calculated if the amplitudes are known. The displacement–traction, since it is a continuous quantity with depth in the reference model, can also be defined for null-thickness layers. Wave amplitudes can thereby be calculated for these layers also.

The analytical continuation consists of using, in each layer of the laterally varying model, the displacements and tractions calculated using the same amplitudes for *P–SV* or *SH* waves as in the reference model, whatever the depth. This ensures that the equation of motion is satisfied in each layer. On the other hand, the continuity conditions between layers are generally not satisfied by the analytical continuation, as sketched in Fig. 3. This discontinuity leads us to introduce surface forces, as indicated in eqs (4) and (5). In the reference model, the amplitudes are, by definition, such that the continuity conditions are satisfied.

Note that there are, in theory, no limits on the lateral changes in the model, even though we use a reference structure to introduce the incident surface wave. In practice, the vertical changes of the location of each interface are limited due to numerical instabilities introduced by the exponential growth in amplitude of the inhomogeneous body waves. This problem increases with frequency and depends strongly on the model, so it is important to verify which frequency interval can be used for any particular model. On the other hand, the boundary conditions are automatically fulfilled in the reference model, so effects due to the horizontal truncation of the model are minimized on the side of the model on which the waves are incident. If the model has the same flat-layered structure on each side of the laterally heterogeneous part, model truncation effects are very small on both sides of the model.

VERIFICATION OF THE METHOD

Choice of verification

To verify the method, we have mostly used incident body waves. In fact, no other complete method is available to simulate surface waves incident on laterally very heterogeneous media, so we have focused on transparency tests and comparisons with known solutions for flat-layered media and simple alluvial basins. In the last part of this section we present a comparison of our method with the coupled local-mode approach for surface waves.

Transparency tests

Transparency tests are the comparison of the analytical solutions of body waves propagating in a half-space with the results of our simulation method applied to multilayered models with irregular interfaces and the same elastic parameters in all layers. We used models with up to four layers and complex interface geometries to verify the correct implementation of the propagator matrices. Using waves incident on the lowermost boundary implies that the surface forces have a significant amplitude everywhere, since they must create the plane waves propagating in all the layers of the model. As a consequence, model truncation effects are significant. We therefore have to use models with flat-layered parts up to 15 times the depth of the deepest interface in order to obtain results within 1–2 per cent of the analytical solutions. To reduce truncation effects, the use of a reference model could be useful for incoming body waves. Simple formulae for transmission and reflection coefficients (e.g. Aki & Richards 1980) would make it possible to create a free field in all layers and therefore minimize the amplitude of the surface forces. We have not implemented this approach, because this study focuses on surface-wave diffraction.

A plane-layered crustal model

The model used for this verification is a two-layered crust on a homogeneous half-space. The elastic properties in the layers are shown in Table 1. We compared our results with results for the reflectivity method (Fuchs 1968; Fuchs & Müller 1971; Kennett & Kerry 1979).

The method was verified for incident *P* and *S* waves with an incidence (θ) relative to the vertical axis of 35° and azimuths (ϕ) of 0° and 40°. Fig. 4 shows a representative example of the results, for an incident *P* wave with 0° azimuth. Our results are shown by solid circles and the reflectivity-method results are shown by continuous lines.

The results are qualitatively similar for both components. Large differences between the reflectivity method and IBEM exist at very low frequencies. This is due to the finiteness of the model in IBEM. At higher frequencies, the two methods yield very similar results, even though small differences exist at some frequencies. These differences are probably due to numerical instabilities and to the differences in the two models, i.e. the model truncation and the finite number of discretization points used in IBEM.

Table 1. Elastic parameters of the three-layer crustal model.

Depth (km)	Vp (km/s)	Vs (km/s)	Rho (g/ cm^3)	Qs=Qp
0-15	6.0	2.6	2.7	10 000
15-40	6.5	2.8	2.8	10 000
40-	8.0	3.4	3.4	10 000

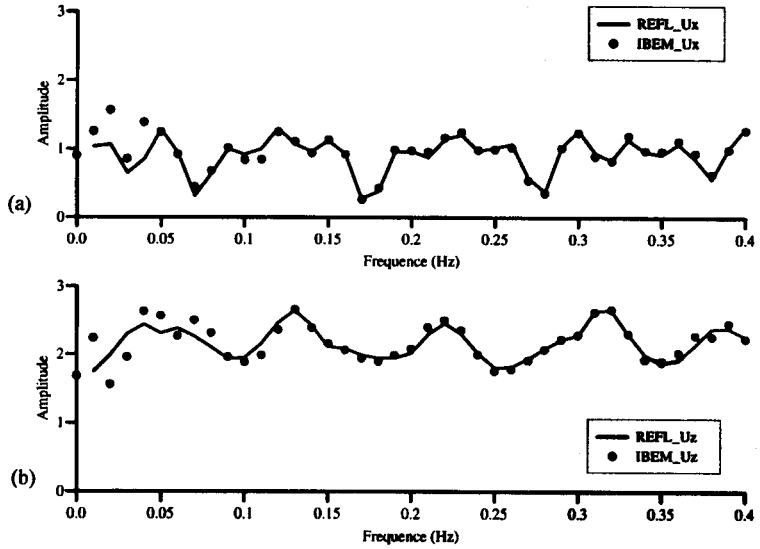

Figure 4. Displacements due to a *P* wave incident on a two-layered crust with a 0° azimuth and a 35° incidence angle. Results from the reflectivity method and IBEM are compared. Solid line: reflectivity method; dots: IBEM. (a) Horizontal component; (b) vertical component.

A simple alluvial valley

We verified our results with those obtained by another IBEM, suitable only for a single inclusion over a half-space (Pei & Papageorgiou 1993; Pedersen *et al.* 1995). The model, shown in Fig. 5, is a simple alluvial valley. To verify the propagator matrices in the multilayer simulations, an additional interface was added at 1 km depth with the same elastic parameters on both sides of the interface. An *SV* wave is incident on this valley with a 30° azimuth and an angle of incidence of 60°. The synthetic seismograms are very similar (within 1 per cent) to those of Pedersen *et al.* (1995). The small differences are probably due to the model truncation effects that exist at low frequencies and to the different model configuration of the two models (the valley is an inclusion in a half-space; the IBEM multilayer is a layer over a half-space). The displacement amplitudes in the frequency–space domain, where differences are easier to identify, are presented in Fig. 6. We show the amplitude of displacement (normalized by the amplitude of the incident *SV* wave) for the three components of motion. The left side of the figure shows results obtained using the simple inclusion method (Pedersen *et al.* 1995) and the right side of the figure shows the results using the multilayer approach. The two methods yield very similar results. Minor differences appear at low frequencies, probably due to model truncation effects, but the agreement is very good at higher frequencies. The similarity of the two sets of spectra was verified by comparing spectra, station by station.

A non-planar crustal model

To verify the implementation of incident surface waves on non-planar structures, we compared our simulations of a fundamental-mode Rayleigh wave incident on a simple crustal model with simulations using the method of coupled local modes (Maupin 1988). The model is shown in Fig. 7. It is a three-layered crust with a thickening of the second layer (centred at $x=100$ km) over a distance of 12.5 km. The elastic parameters are shown in Table 2. A smooth model was chosen in order to minimize conversions of surface waves to body waves, which are not taken into account by the method of coupled local modes.

Fig. 8 shows the comparison between the two methods for a Rayleigh wave that is perpendicularly incident on the structure from the left. The source function is a Ricker wavelet of 5 s central period. The comparison is shown for the horizontal and vertical components at three locations: at $x=50$ km, (to the left of the heterogeneity), $x=100$ km (above the centre of the heterogeneity), and $x=150$ km (to the right of the heterogeneity).

Both methods show that only a very small fraction of energy is back-scattered as Rayleigh waves, which are very

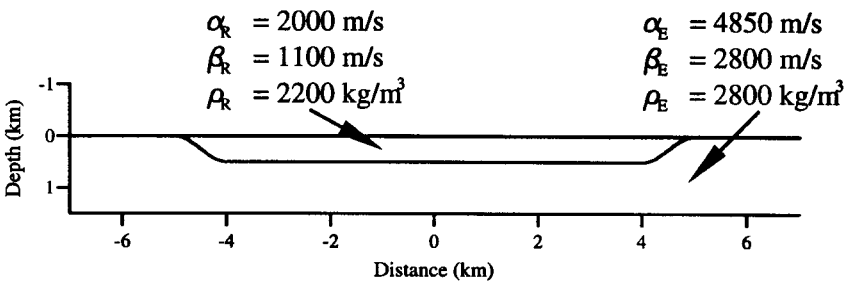

Figure 5. Model of a simple alluvial valley used in the verifications. The elastic parameters (*P*-wave velocity, α, *S*-wave velocity, β, and density, ρ) are shown for the valley (supscript R) and the half-space (subscript E).

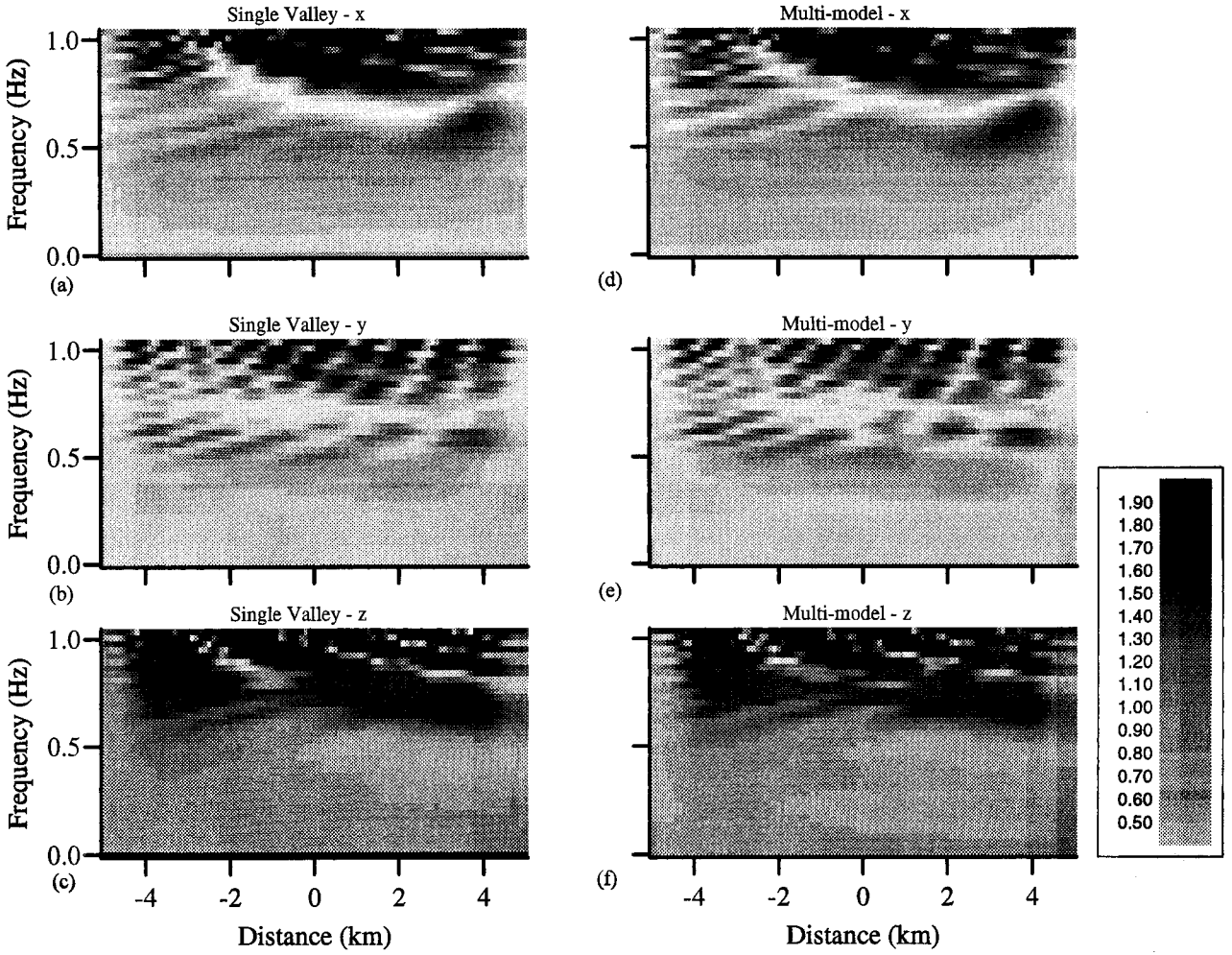

Figure 6. Spectral response of an alluvial valley obtained by multilayer IBEM and a simple valley IBEM for incident *SV* waves with an azimuth of 30° and incidence of 60°. (a) Single valley, *x* component; (b) single valley, *y* component; (c) single valley, *z* component; (d) multilayer, *x* component; (e) multilayer, *y* component; (f) multilayer, *z* component.

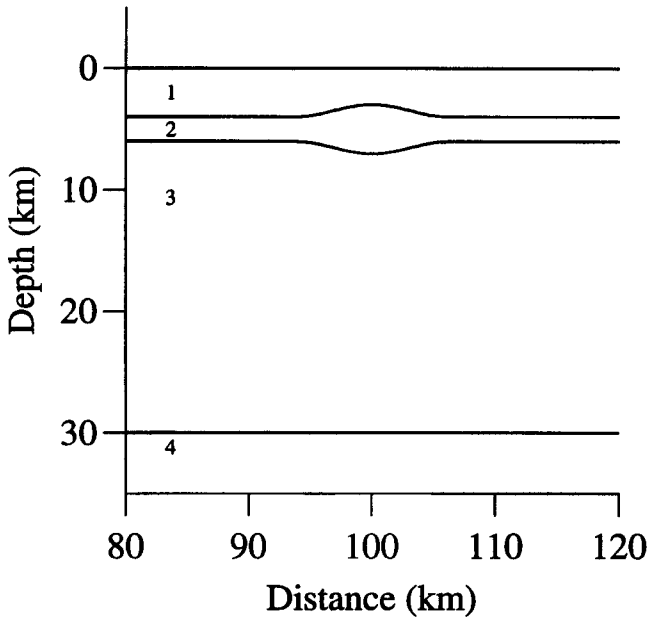

Figure 7. Irregular crustal model used for comparison with the coupled local-mode approach.

Table 2. Elastic parameters of the crustal model of Fig. 7.

Layer No	Vp (km/s)	Vs (km/s)	Rho (g/cm^3)
1	2.5	1.5	1.5
2	4.0	2.5	2.0
3	6.5	3.7	2.7
4	8.0	4.7	3.1

low-amplitude waves, indicated in Fig. 8 by an arrow. For IBEM, body-wave energy may also be present. The amplitude ratio of the back-scattered waves of the two methods is less than two. We consider this acceptable because at least part of this value can be accounted for by the exclusion, in the coupled local-mode approach, of body waves that are not trapped in the structure. The phase changes of the forward-propagating Rayleigh waves due to the heterogeneous structure are similar in the two calculation methods.

It is very difficult to estimate how much energy is propagated as body waves and how much as surface waves because IBEM yields the total wavefield without separation of different wave types during the calculation.

APPLICATION TO THE SORGENFREI–TORNQUIST ZONE

Model

In this section, we present numerical simulations of fundamental-mode Rayleigh waves incident on a major lithospheric boundary. The example, presented in Fig. 9, was chosen to complement the results of Pedersen *et al.* (1994), who identified a major change in lithospheric structure across the Sorgenfrei–Tornquist Zone (STZ) in southern Scandinavia by analysis of Rayleigh-wave dispersion. They propose two different flat-layered lithospheric models north and south of the STZ. Their model north of the STZ presents no major low-velocity layer, while the model south of the STZ has a significant low-velocity layer below a depth of 100 km. We connect the two types of lithosphere in the geometrically simplest way with a 400 km wide transition zone. The elastic parameters of the model are shown in Table 3. No well-constrained model is available for the area, so the model used in the simulations is simply aimed at studying diffraction effects of Rayleigh waves by such a sharp and significant lithospheric boundary.

Table 3. Elastic parameters of the lithospheric model of Fig. 9.

Layer No	Vp (km/s)	Vs (km/s)	Rho (g/cm^3)
1	5.5	3.12	2.5
2	6.4	3.42	2.7
3	6.8	4.06	2.8
4	8.0	4.43	3.2
5	8.1	4.80	3.3
6	8.2	4.46	3.4
7	8.2	4.23	3.4
8	8.2	4.82	3.4

For the simulations, each interface of the model is discretized with at least five points per wavelength, and a minimum of 450 points to represent the central geometry of the structure well. The simulations were carried out for frequencies between 0 and 0.04 Hz, in a time window of 1000 s. We verified that the incident wavefield was stable in this frequency interval, i.e. that the analytically extended expressions of up- and down-going P and SV waves showed no numerical instabilities in any layer.

Synthetic seismograms

We perform numerical simulations for fundamental-mode Rayleigh waves incident perpendicularly or obliquely on the structure in Fig. 9. The calculations are carried out in the frequency domain and synthetic seismograms are obtained by multiplication with a source function, followed by a Fourier transform. The ground movement is simulated along a 2000 km long profile, with 800 km on each side of the 400 km wide transition zone.

Fig. 10 shows the synthetic seismograms for Rayleigh waves perpendicularly incident (i.e. 0° azimuth) on the structure from the south. The amplitudes are multiplied with the same value in Figs 10(a) and (b), so the amplitude ratio between the two components is respected. The source function is a Ricker wavelet with an 80 s central period. The Rayleigh waves propagate across the structure while being slowly altered according to the local dispersion properties of the medium. Magnification of the seismograms (Fig. 10c, magnified 100 times) nevertheless reveals the presence of back-scattered energy. On the horizontal component these waves have ~0.5–1 per cent amplitude relative to the incident waves. Some of these waves have an apparent propagation velocity of ~8 km s^{-1}, so they are identified as P waves (arrow 1 in Fig. 10). The other back-scattered waves propagate with a velocity of ~4 km s^{-1} (arrow 2 in Fig. 10). They are probably a mixture of S waves and reflected Rayleigh waves, but the time separation between the different types of back-scattered waves is too small to perform a reliable polarization analysis. There is also some indication of forward-scattered P waves (arrow 3 in Fig. 10a).

The scattered waves distort the waveforms, particularly in the transition zone. This influences phase-velocity measurements, which we discuss in the next subsection.

Fig. 11 shows synthetic seismograms for fundamental-mode

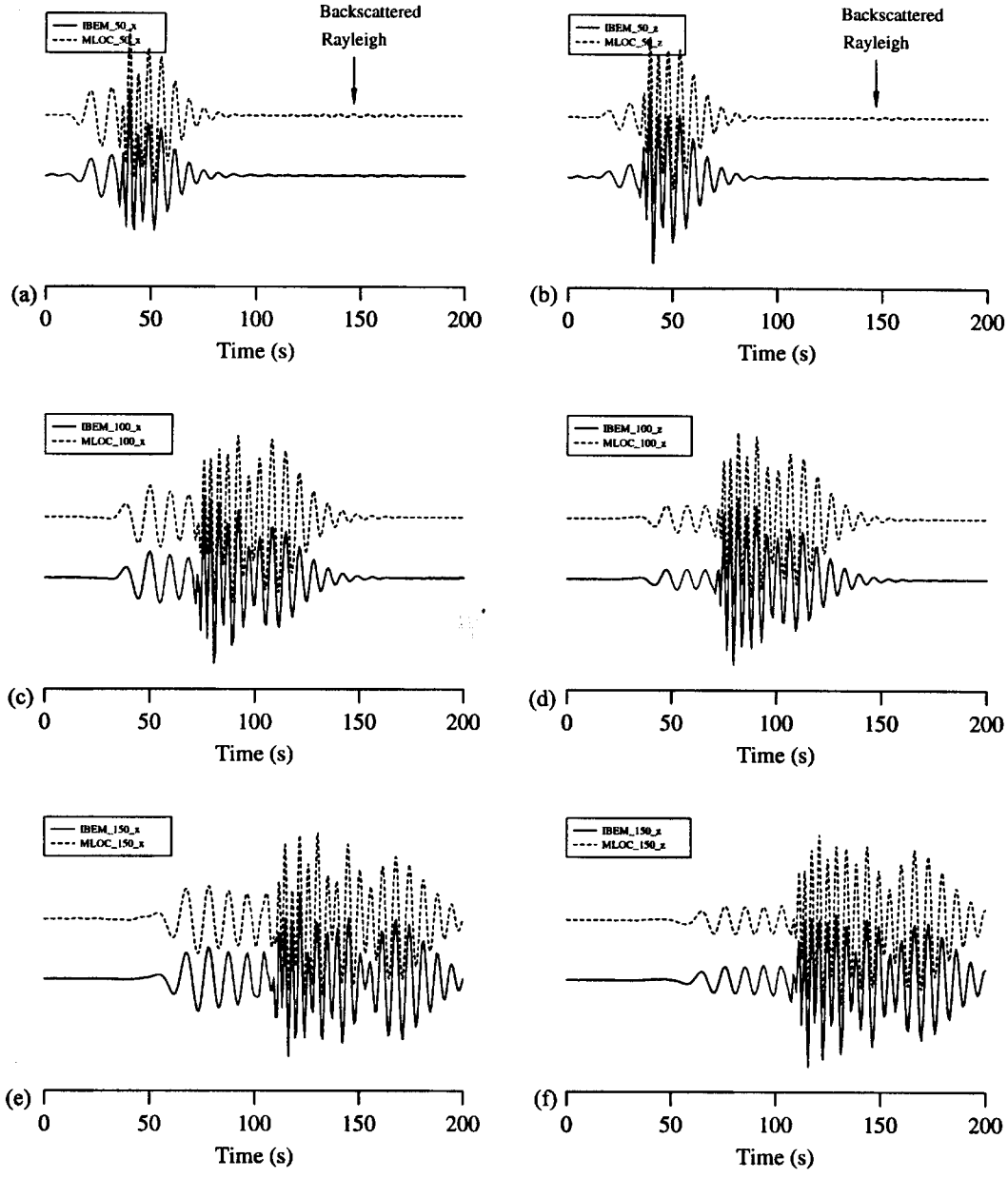

Figure 8. Comparison of displacements due to a fundamental-mode Rayleigh wave incident on the irregular crustal structure of Fig. 7. Solid lines: IBEM; dashed lines: method of local coupled modes ('MLOC'). Results are shown for three locations: to the left, above, and to the right of the heterogeneity. (a) $x=50$ km, x component; (b) $x=50$ km, z component; (c) $x=100$ km, x component; (d) $x=100$ km, z component; (e) $x=150$ km, x component; (f) $x=150$ km, z component. The arrow indicates the presence of back-scattered waves.

Rayleigh waves incident upon the structure from the north with an azimuth of 30°. The horizontal components are rotated 30°, so we present the 'radial', 'tangential' and vertical components. The rotation yields the proper radial and tangential components of the incident Rayleigh wave north of the structure. South of the structure, the change in propagation velocity induces a change in propagation angle, which is different for Love and Rayleigh waves, so the waves cannot be completely separated. The same problem is present for the back-scattered Rayleigh and Love waves, but it is, however, possible to estimate the horizontal displacement amplitude ratios (scattered/incident waves) because the direction of propagation of the Rayleigh waves is known. The estimation showed that this ratio for back-scattered Rayleigh waves is 0.6 per cent and that it is 2 per cent for back-scattered Love waves.

In this example, there are no significant back-scattered P waves. The diffraction by the heterogeneity mainly yields back-scattered surface waves and significant energy conversion towards forward-scattered Love waves. However, the fundamental-mode Rayleigh wave remains stable across the heterogeneity.

The Earth's sphericity is not accounted for in the calculations presented here. It would be accounted for better by using a model that is locally the flattening transformation of the spherical one. Considering the results of Maupin (1992) for a surface-wave study at the same scale as that conducted here,

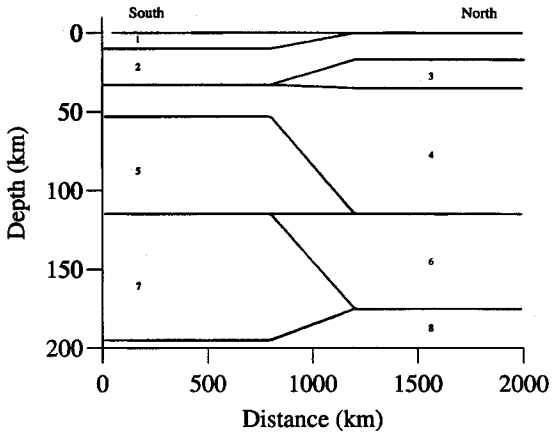

Figure 9. Simple model of the Sorgenfrei–Tornquist Zone, as used in the simulations. The profile is 2000 km long, with a 400 km wide transition zone in the centre.

we expect that accounting for the Earth's sphericity would not significantly modify the relative amplitudes of the scattered waves, and thereby our conclusions.

Phase-velocity analysis

In this subsection we investigate how the interaction between direct and diffracted waves influences the apparent phase velocity measured at the surface across the array.

We choose to simulate a measurement that is not limited by the number of stations present at the surface. We also choose to analyse records of vertical movement to eliminate the influence of Rayleigh- to Love-wave conversions and to minimize the influence of the diffracted waves, which is smaller on the vertical component than on the horizontal component. The phase velocities that we present are therefore based on ideal conditions, so the phase velocities that we measure on the synthetic seismograms are biased only by the earth structure and not by the quality of the measurement.

We measure nine phase-velocity dispersion curves across the array, along profiles 400 km in length. Each profile overlaps its neighbouring profiles by 200 km, i.e. the profiles are located at 0–400 km, 200–600 km, ..., 1600–2000 km. The measured dispersion curves are attributed to the centre of each profile.

In the following discussion, we compare the measured dispersion curves to the 'local' dispersion, i.e. the dispersion curve of a fundamental-mode Rayleigh wave propagating in a flat-layered earth with the local elastic parameters. If the measured dispersion curve is similar to the local one it is possible to retrieve the local earth structure by classical inversion procedures. Otherwise, one may obtain an earth structure very different from the real one.

We verified the stability of different methods of measuring phase velocities by comparing the measured dispersion curves with the theoretical ones. Slant stack performed over the 21 stations of each profile yields the best stability and is therefore used systematically to measure dispersion curves using the synthetic seismograms.

Fig. 12 shows the phase velocities measured on the vertical components of the seismograms in Fig. 11. The nine dispersion curves are represented on the same diagram, so it is possible to follow their evolution across the array. For the purpose of

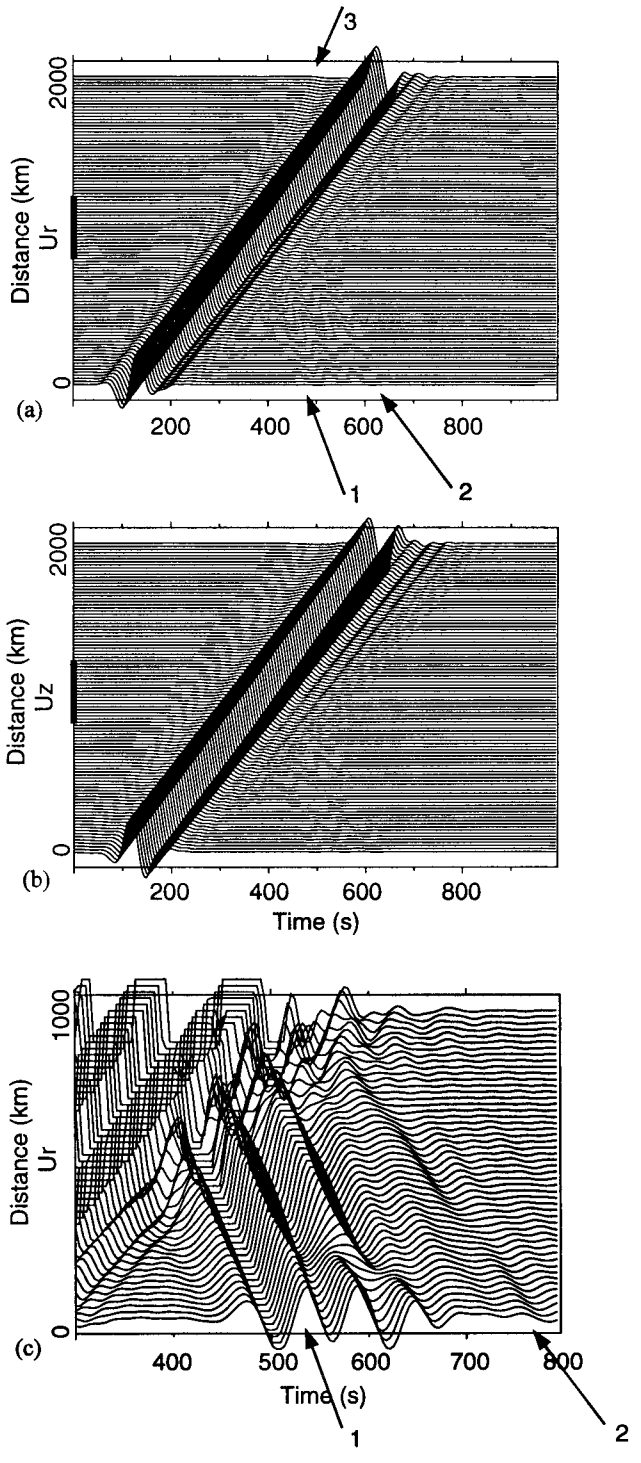

Figure 10. Synthetic seismograms for Rayleigh waves incident from the south with a 0° azimuth on the Sorgenfrei–Tornquist Zone. The arrows indicate the seismic phases discussed in the main text, with arrow 1 showing back-scattered *P* waves, arrow 2 showing back-scattered *S* or Rayleigh waves, and arrow 3 showing a possible forward-scattered wave. The bold line in the centre of the distance scale of (a) and (b) indicates the Sorgenfrei–Tornquist Zone. (a) Horizontal component; (b) vertical component; (c) section of the horizontal component magnified 100 times to show details of the back-scattered waves (arrows 1 and 2).

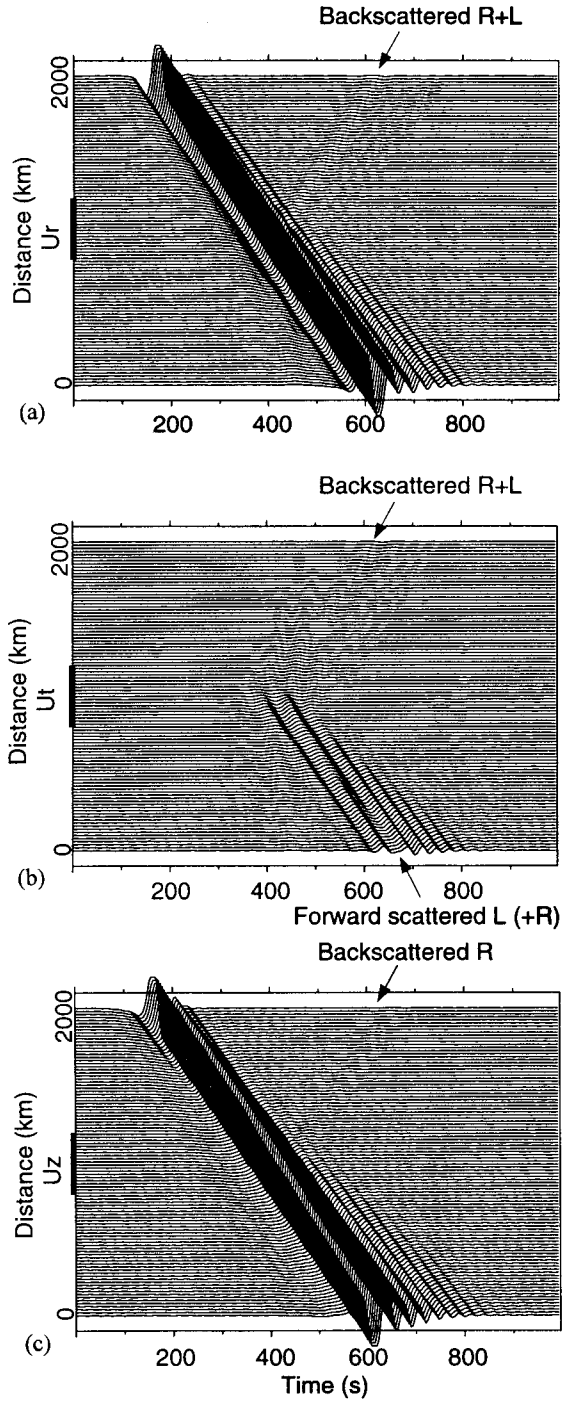

Figure 11. Synthetic seismograms for Rayleigh waves incident from the north with a 30° azimuth. The amplitude scale is the same as in Figs 10 (a) and (b) The rotation of the horizontal components is discussed in the text. The location of the Sorgenfrei–Tornquist Zone is indicated by a bold line in the centre of each distance scale. (a) 'Radial' component; (b) 'transverse' component; (c) vertical component.

3-D perspective, a 3-D surface was fitted to the nine curves. The bold lines represent the local dispersion curves at $x=$ 0 km (south of the transition zone) and at $x=2000$ km (north of the transition zone). Note that as the transition zone is only 400 km wide, the three southernmost profiles, as well as the three northernmost ones, are measured in laterally homogeneous regions.

The figure clearly shows how the dispersion curves measured at the surface fluctuate significantly across a major transition zone, such as the one used in our simulations. The fluctuations of the dispersion curves are up to 2 per cent of the average phase velocity, but they are higher when a two-station measurement is used. The measured dispersion curves fit well with the theoretical ones north of the transition zone, i.e. where the Rayleigh waves are incident, but they fluctuate significantly in and beyond the transition zone. This difference can be attributed to two causes. First, the time separation is better between the incident Rayleigh waves and the back-scattered waves than between the Rayleigh waves and the forward-scattered waves. Second, the amplitude of the back-scattered waves may be smaller than that of the forward-scattered waves. However, it is possible to measure the phase velocities of the incident and back-scattered waves independently if they are well separated in time, even when the back-scattered waves have high amplitudes.

CONCLUSIONS

IBEM is a promising tool for simulating seismic-wave propagation in strongly heterogeneous media. It takes into account the total wavefield with all conversions between wave types. The main disadvantage of IBEM is that a large matrix must be inverted at least once during the calculation. The size of the matrix defines the practical limit of the calculation towards the high frequencies because the number of discretization points increases with frequency. The inversion of large matrices is also responsible for the long CPU time at high frequencies.

The generalization of IBEM to the case of irregularly multilayered media does not increase the size of the matrices that need to be inverted compared to a single layer over a half-space, and the CPU time increases approximately linearly with the number of layers. The simulation of Rayleigh waves incident on the Sorgenfrei–Tornquist Zone consumed $\sim$50 hr CPU time on an IBM RISC 6000 workstation, and it used up to 400 megabytes of memory during the calculation.

The formulation that we use is very flexible and the possibility of superposing interfaces is useful for taking into account geometrically complex media. We separate the recursive formulae of the free field from those of the diffracted field, so it is very easy to include other types of wave excitation than the ones considered here. For 3-D diffraction by 2-D structures, the incoming waves must be plane to maintain the advantages of this specific approach. In other cases (pure 2-D or full 3-D) it is straightforward to introduce, for example, an earthquake source. With the formulation presented, it is also relatively easy to extend the method to 3-D geometries.

Very different simulation problems can be considered, from site effects to wave propagation in lithospheric models, and with body waves as well as surface waves incident upon the structure. IBEM can be used with the present generalization to gain a better understanding of seismic diffraction by strongly heterogeneous media and to model data by either trial and error or non-linear inversion using very simple models.

The application to the diffraction of long-period surface waves by a strong heterogeneity in the upper mantle shows that the local fluctuations of dispersion curves should not be interpreted in terms of a flat-layered earth. A strong smoothing

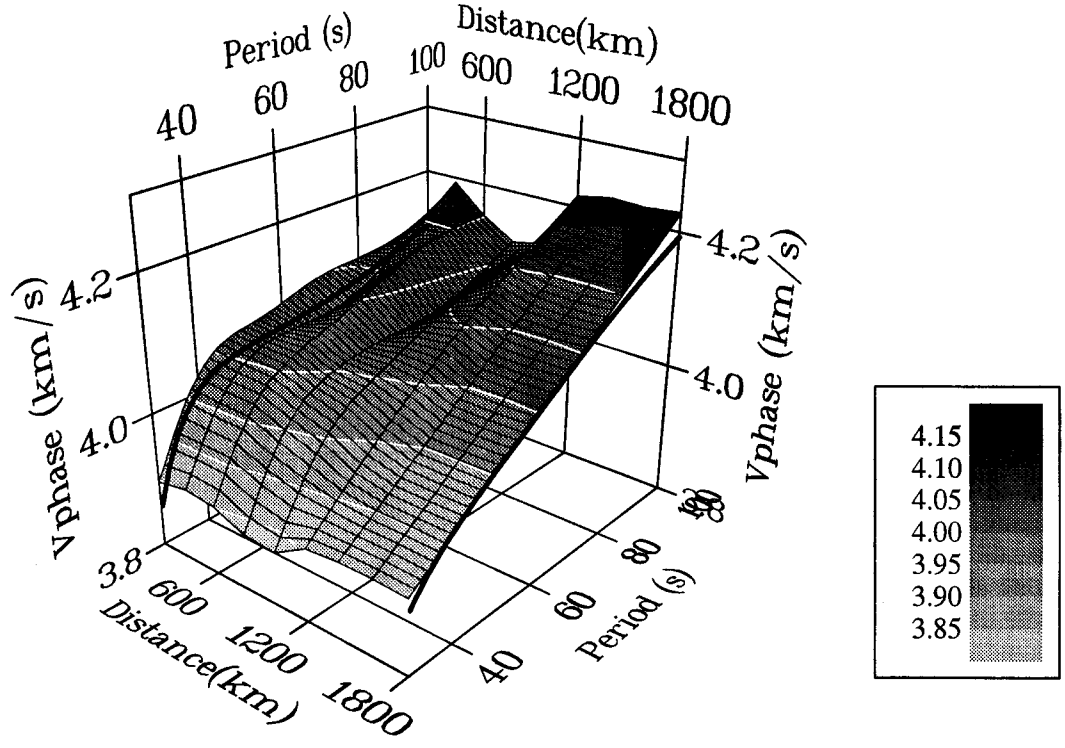

Figure 12. Phase-velocity dispersion curves measured on the seismograms of Fig. 11 (c) The shaded 3-D surface shows the nine dispersion curves measured on the synthetic seismograms. The two bold lines are the dispersion curves of the local fundamental mode north and south of the transition zone.

of dispersion curves is necessary in this case in order to obtain a local earth model, which is possibly biased. On the other hand, it confirms that surface waves can be used to detect strong heterogeneities in the lithospere.

ACKNOWLEDGMENTS

All IBEM calculations were carried out at the Centre de Calcul Intensif at the Observatoire de Grenoble. One of the authors (VM) was supported by Norges Forskningsraad. The project received support from the European Community under research grant B/EPOCH-913006. We thank an anonymous reviewer for pointing out several imprecisions in the original text.

REFERENCES

Aki, K. & Richards, P.G., 1980. *Quantitative seismology,* W.H. Freeman, San Francisco, CA.

Ben Menahem, A.B.-M. & Singh, S.J., 1981. *Seismic waves and sources,* Springer Verlag, Berlin.

Bouchon, M., Campillo, M. & Gaffet, S., 1989. A boundary integral equation–discrete wavenumber representation method to study wave propagation in multilayered media having irregular interfaces, *Geophysics,* **54,** 1134–1140.

Cao, S. & Muirhead, K.J., 1993. Finite difference modelling of Lg blockage, *Geophys. J. Int.,* **115,** 85–96.

Drake, L.A. & Bolt, B.A., 1989. Finite element modelling of surface wave transmission across regions of subduction, *Geophys. J. Int.,* **98,** 271–279.

Fitas, A.J.S. & Mendes-Victor, L.A., 1992. Rayleigh waves normally incident at a continental boundary, *Geophys. J. Int.,* **109,** 171–182.

Fuchs, K., 1968. The reflection of spherical waves from transition zones with arbitrary depth-dependent elastic moduli and density, *J. Phys. Earth,* **16,** 27–41.

Fuchs, K. & Müller, G., 1971. Computations of synthetic seismograms with the reflectivity method and comparison with observations, *Geophys. J.R. astr. Soc.,* **23,** 417–433.

Gregersen, S., 1978. Possible mode conversion between Love and Rayleigh waves at a continental boundary, *Geophys. J.R. astr. Soc.,* **54,** 121–127.

Kennett, B.L.N., 1984. Guided-wave propagation in laterally varying media. I. Theoretical development, *Geophys. J.R. astr. Soc.,* **79,** 235–255.

Kennett, B.L.N. & Kerry, N.J., 1979. Seismic waves in stratified half spaces, *Geophys. J.R. astr. Soc.,* **57,** 557–583.

Kupradze, V.D., 1963. Dynamical problems in elasticity, in *Progress in Solid Mechanics,* Vol. III, pp. 191–255, eds Sneddon, I.N. & Hill, R., North-Holland, Amsterdam.

Lysmer, J. & Drake, L.A., 1972. A finite element method for seismology, in *Methods of Computational Physics,* Vol. 11, pp. 181–216, ed. Bolt, B.A., Academic Press, New York, NY.

Maupin, V., 1988. Surface waves across 2-D structures: a method based on coupled local modes, *Geophys. J.,* **93,** 173–185.

Maupin, V., 1992. Modelling of laterally trapped surface waves with application to Rayleigh waves in the Hawaiian swell, *Geophys. J. Int.,* **110,** 553–570.

McGarr, A. & Alsop, L.E., 1967. Transmission and reflection of Rayleigh waves at vertical boundaries, *J. geophys. Res.,* **72,** 2169–2180.

Nolet, G., Grand, S.P. & Kennett, B.L.N., 1994. Seismic heterogeneity in the upper mantle, *J. geophys. Res.,* **99,** 23 723–23 766.

Pedersen, H.A., Sánchez-Sesma, F.J. & Campillo, M., 1994. Three-dimensional scattering by two-dimensional topographies, *Bull. seism. Soc. Am.,* **84,** 1169–1183.

Pedersen, H.A., Campillo, M. & Sánchez-Sesma, F.J., 1995. Azimuth dependent wave amplification in alluvial valleys, *Soil Dyn. Earthq. Eng.,* **14,** 289–300.

Pei, D. & Papageorgiou, A.S., 1993. Study of the response of cylindrical alluvial valleys of arbitrary cross-section to obliquely incident seismic waves using the discrete wavenumber boundary element method, in *Soil Dynamics and Earthquake Engineering,* vol VI, pp. 149–161, eds Cakmak, A.S. & Brebbia, C.A., Comp. Mech. Publications, Elsevier Applied Science, Boston.

Sánchez-Sesma, F.J. & Campillo, M., 1991. Diffraction of P, SV and Rayleigh waves by topographical features: a boundary integral formulation, *Bull. seism. Soc. Am.,* **81,** 2234–2253.

Sánchez-Sesma, F.J. & Campillo, M., 1993. Topographic effects for incident P, SV and Rayleigh waves, *Tectonophysics,* **218,** 113–125.

Sánchez-Sesma, F.J. & Luzón, F., 1995. Seismic response of three-dimensional alluvial valleys for incident P, S and Rayleigh waves, *Bull. seism. Soc. Am.,* **85,** 269–284.

Sánchez-Sesma, F.J., Ramos-Martinez, J. & Campillo, M., 1993. An indirect boundary element method applied to simulate the seismic response of alluvial valleys for incident P, S, and Rayleigh waves, *Earthq. Eng. Struct. Dyn.,* **22,** 279–295.

Snieder, R., 1986. 3-D linearized scattering of surface waves and a formalism for surface wave holography, *Geophys. J.R. astr. Soc.,* **84,** 581–605.

Stange, S. & Friederich, W., 1992a. Guided wave propagation across sharp lateral heterogeneities: the complete wavefield at plane vertical discontinuities, *Geophys. J. Int.,* **109,** 183–190.

Stange, S. & Friederich, W., 1992b. Guided wave propagation across sharp lateral heterogeneities: the complete wavefield at a cylindrical inclusion, *Geophys. J. Int.,* **111,** 470–482.

Woodhouse, J. & Dziewonski, A.M., 1984. Mapping the upper mantle: three-dimensional modeling of earth structure by inversion of seismic waveforms, *J. geophys. Res.,* **89,** 5 953–5 986.